




Modeling Ice Shelf Cavities and Tabular Icebergs Using Lagrangian Elements

A. A. Stern¹ , A. Adcroft¹ , and O. Sergienko¹ 

¹Atmospheric and Oceanic Sciences, Princeton University, Princeton, NJ, USA

Key Points:

- A novel modeling framework is developed to simulate ice shelves calving icebergs using Lagrangian elements, held together by numerical bonds
- After an iceberg calves away from an ice shelf, a complex interaction is observed between the iceberg motion and ocean hydrography
- A Taylor column, subsurface cooling at the ice front, and reduced melt rates within the ice-shelf cavity are observed after iceberg calving

Supporting Information:

- Supporting Information S1
- Figure S1
- Figure S2
- Figure S3
- Figure S4
- Figure S5
- Movie S1
- Movie S2

Correspondence to:

A. A. Stern,
sternalon@gmail.com

Citation:

Stern, A. A., Adcroft, A., & Sergienko, O. V. (2019). Modeling ice shelf cavities and tabular icebergs using lagrangian elements. *Journal of Geophysical Research: Oceans*, 124, 3378–3392. <https://doi.org/10.1029/2018JC014876>

Received 21 DEC 2018

Accepted 14 APR 2019

Accepted article online 23 APR 2019

Published online 28 MAY 2019

Abstract Most ocean climate models do not represent ice shelf calving in a physically realistic way, even though the calving of icebergs is a major component of the mass balance for Antarctic ice shelves. The infrequency of large calving events together with the difficulty of placing observational instruments around icebergs means that little is known about how calving icebergs affect the ocean. In this study we present a novel model of an ice shelf coupled to an ocean circulation model, where the ice shelf is constructed of Lagrangian elements that allow simulation of iceberg calving. The Lagrangian ice shelf model is used to simulate the flow beneath a static idealized ice shelf, to verify that it can reproduce the results of an existing Eulerian model simulation with an identical configuration. The Lagrangian model is then used to simulate the ocean's response to a calved iceberg drifting away from the ice shelf. The results show how a calving event and subsequent iceberg drift affect the ocean. At the ice front, the calving event leads to a warming of the ocean surface and cooling of the water column at depth, allowing cooler waters to enter the ice shelf cavity, leading to reduced melt rates within the cavity. A Taylor column is observed below the iceberg, which moves with the iceberg as it drifts into the open ocean. As the iceberg drifts further from the ice shelf, the circulation within the ice shelf cavity tends toward a new steady state, consistent with the new ice shelf geometry.

1. Introduction

Satellite observations show that ice shelf mass loss occurs via two main processes, subaquatic melting and iceberg calving (Depoorter et al., 2013; Rignot et al., 2013), that contribute approximately equally. Each process influences the surrounding ocean (and ice shelf geometry) in a distinct way. Melting at the base of ice shelves fluxes freshwater into the ice shelf cavity. The input of buoyant melt water creates rising density plumes, which are guided along the ice shelf base, and help drive ocean circulation beneath the ice shelves (Holland & Feltham, 2006; MacAyeal, 1984). Over time, melting at the ice shelf base gradually alters the ice shelf geometry. In contrast, calving of the ice shelf front causes sudden changes to the ice shelf geometry. Large calving events can release giant tabular icebergs into the ocean. After calving, these tabular icebergs can travel large distances and impact ocean hydrography (Martin & Adcroft, 2010; Stern et al., 2015), sea ice formation (Robinson & Williams, 2012; Stern et al., 2016; Wagner et al., 2018), and ocean biology (Biddle et al., 2015; Smith et al., 2007; Vernet et al., 2012) far from the calving location.

Modeling the ocean beneath the ice shelves presents a unique set of challenges, since (i) the presence of ice shelves provides a quasi-rigid upper boundary for the ocean model, which is not encountered elsewhere in the ocean, and (ii) grounding-line motion, as well as thickness change and fracturing of ice shelves, implies changing ocean boundary conditions that present numerous numerical difficulties.

The earliest models of ocean cavities under ice shelves were developed using static ice shelves with a fixed shape (Determann & Gerdes, 1994; Grosfeld et al., 1997; Hellmer & Olbers, 1989; Holland & Jenkins, 2001; Losch, 2008). In these models, ice shelf melting was represented through salinity and temperature fluxes. Later models of ice shelf cavities allowed the ice shelf geometry to evolve, permitting the study of coupled ocean-ice phenomena (Gladish et al., 2012; Sergienko, 2013). Dynamic ice shelf models have also been coupled to the ocean cavity, allowing the study of grounding line migration, which is of key importance for sea level rise projections (DeRydt & Gudmundsson, 2016; Goldberg et al., 2012; Grosfeld & Sandhger, 2004; Seroussi et al., 2017; Timmermann & Goeller, 2017).

All models of ice shelf cavities to date have omitted ice shelf rifting and iceberg detachment. This is because (i) there is much uncertainty about the physics that govern ice shelf rifting (Alley et al., 2008; Bassis &

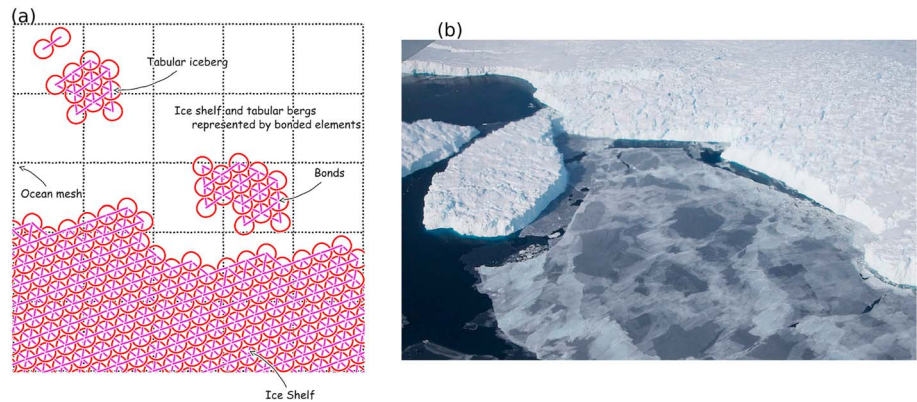


Figure 1. Schematic showing Lagrangian elements representation of ice shelves and tabular icebergs. (a) Schematic of multiple ice elements joined together by numerical bonds (magenta lines) to form larger structures such as ice shelves and tabular icebergs. (b) Aerial photograph of an ice shelf and tabular iceberg for comparison.

Jacobs, 2013; Benn et al., 2007; Levermann et al., 2012) and (ii) current models of ice shelf cavities represent the ice shelves on static Eulerian grids, which do not lend themselves to modeling iceberg detachment and drift. In contrast, existing *iceberg* models represent icebergs as Lagrangian particles, which is the natural way to model objects traveling over large distances (Bigg et al., 1997; Gladstone et al., 2001; Marsh et al., 2015; Martin & Adcroft, 2010). To date, there have been no attempts to synthesize these two approaches (i.e., to combine ice shelf and iceberg models).

In this study we develop a new ice shelf model where the ice shelf is simulated with Lagrangian elements that are bonded together by numerical bonds (Figure 1). This Lagrangian framework allows for large pieces of the ice shelf to break away and become tabular icebergs. An example of this enhanced capability of the Lagrangian model is demonstrated in Figure 2, which shows a tabular iceberg drifting away from an idealized ice shelf. This Lagrangian modeling technique was used by Stern et al. (2017) to model tabular icebergs and is extended in this study to model ice shelves with calving icebergs. Here we (i) introduce and describe the Lagrangian ice shelf model, (ii) verify that the Lagrangian model simulating the flow beneath a static idealized ice shelf cavity can reproduce the results of an Eulerian ice shelf model run in an identical configuration, and (iii) demonstrate the enhanced capabilities of the Lagrangian ice shelf model by simulating a large iceberg calving away from the idealized ice shelf. Modeling the ocean during and after a calving event allows us to observe how the calving event affects the ocean near and beneath the ice shelf and how changes in the ocean feedback onto the ice shelf.

2. Lagrangian Model Description

The Kinematic Iceberg Dynamics (KID) model is a Lagrangian model that was developed to simulate tabular icebergs (Stern et al., 2017). Here, we use the same methods to simulate the ice shelf during a calving event, coupled to an ocean model simulating the ice shelf cavity. The model represents ice shelves using Lagrangian elements joined together by numerical bonds. By breaking these bonds, the model is able to simulate ice shelf calving and iceberg breakup.

In this section we describe the Lagrangian ice shelf model. A more complete description of the model including numerical methods and algorithms used to track the numerical bonds can be found in Stern et al. (2017).

2.1. KID Model

In the KID model, each Lagrangian element represents a column of ice that is floating in the ocean. The elements each have their own position, velocity, mass, and a set of spatial dimensions, which can evolve in time. Each element moves according to its own momentum balance, which is computed in the (Lagrangian) reference frame of the element. The elements experience drag forces from the ocean, atmosphere, and sea ice; forces due to sea surface height gradients; and the Coriolis force (Bigg et al., 1997; Gladstone et al., 2001; Martin & Adcroft, 2010; Stern et al., 2017). The elements also interact with other elements and can be connected by numerical bonds, which allow elements to move together as a unit. By bonding many ice

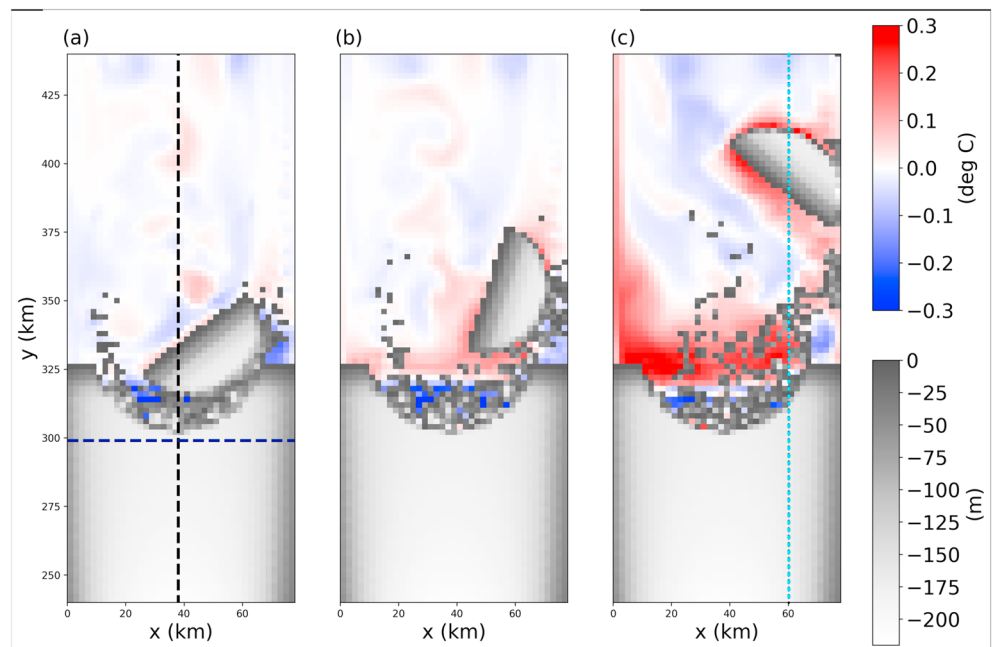


Figure 2. Snapshots of sea surface temperature anomalies in the iceberg-calving simulation (section 5.1). The anomalies are relative to precalving temperatures. Snapshots are taken (a) 7, (b) 15, and (c) 50 days after calving. Grid cells with ice mass $> 10^4$ kg are plotted in white, with gray shading indicating thinner ice. The black and blue dashed lines in panel (a) and the dashed line in panel (c) show the location of the vertical transects in Figures 6 and 9a; Figure 7; and Figures 9b, 9c, and 9d, respectively.

elements together, the model is able to represent large structures, such as tabular icebergs or ice shelves (Figure 1).

The momentum equations and a description of the interactive forces between elements are provided in the supporting information.

2.2. Parameterization of Melt Rates

The thickness and extent of the Lagrangian elements change due to melting when they are exposed to above-freezing ocean mixed-layer temperatures. The melt rates of the elements in the interior of a large structure (such as an ice shelf or large icebergs) are parameterized using the three-equation model, which is a typical melt rate parameterization used to model basal melt beneath ice shelves (Holland & Jenkins, 1999). The melt rates of freely floating ice elements (not bonded to other elements) are parameterized using standard parameterizations for iceberg melt (Bigg et al., 1997; Gladstone et al., 2001; Martin & Adcroft, 2010). For elements at the edge of large structures (with edges partly exposed to the open ocean), the melt rates are computed using a weighted sum of the ice shelf and iceberg melt rate parameterization, with the weights being proportional to the fraction of the element's perimeter, which exposed to the open ocean (Stern et al., 2017).

2.3. Initializing Element Geometry and Packing

The elements in the Lagrangian model are shaped as equal-sized regular hexagons (although they are treated as circular for the purpose of element interactions). We initialize the Lagrangian model by positioning the elements in a staggered lattice of equal-sized hexagons, so that the elements fit together and perfectly tile the ice shelf surface (Figure 1). Smaller hexagonal elements are added to fill gaps along the edges of the domain. Hexagonal elements are used so that when adjacent pairs of elements are bonded together, the network of bonds form equilateral triangles, which gives rigidity to the larger structure (Stern et al., 2017). By using hexagonal elements, which can be packed together without any gaps, the element initialization is perfectly space filling. This allows the model to simulate continuous ice shelves (without gaps or crevasses) and allows the results to be more easily comparable with Eulerian ice shelf models. In this study, we only use hexagonal elements; however, other element geometries can be used when less precision is needed.

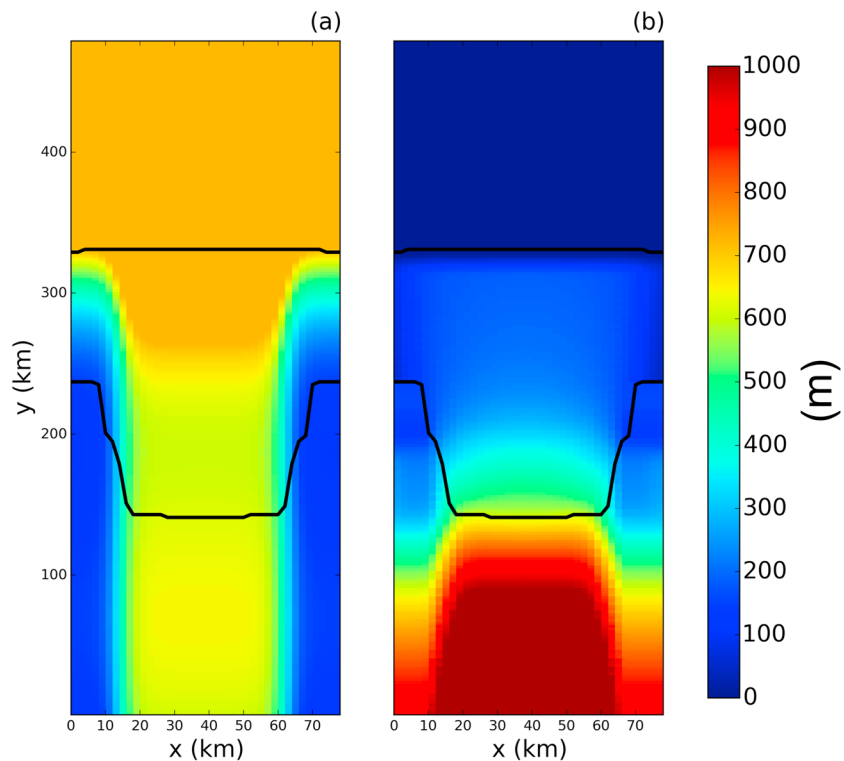


Figure 3. Model geometry. (a) Ocean bottom topography and (c) ice shelf draft used to initialize the static ice shelf experiment simulations. The lower and upper black lines denote the grounding line and ice shelf front, respectively.

2.4. Interpolation and Aggregation Onto the Lagrangian Grid

The KID model is coupled to the ocean model via a two-way synchronous coupling, meaning that ocean model fields are passed through the Coupler to the KID model and KID model fields are passed back through the Coupler to the ocean model at every time step. Fields that are passed from the ocean model to the Lagrangian ice shelf model have to be interpolated from the Eulerian grid onto the Lagrangian grid (i.e., to the elements). This is done using a bilinear interpolation scheme. Four ocean fields are passed from the ocean model to the ice shelf model: temperature, salinity, and zonal and meridional velocities. At the end of an ice shelf model time step, ice shelf fields are aggregated from the elements back onto the Eulerian ocean grid and are then passed from the ice shelf model to the ocean model. The aggregation is done by calculating the fraction of each element's volume that lies in each ocean grid cell and dividing the fields in proportion to this fraction. For example, the amount of ice mass aggregated onto a given ocean grid cell is found by summing up the masses of all elements that intersect that grid cell, only counting the part of an element's mass that actually intersects the ocean grid cell. When calculating the intersection between an element and a grid cell, we assume that the elements have surface areas that are shaped as regular hexagons. Seven fields are passed from the ice shelf models to ocean model: iceberg mass and surface area (used to calculate the weight exerted on the ocean), temperature flux, salinity flux and mass flux, and meridional and zonal velocity (used to calculate the momentum flux).

3. Experiment Setup

3.1. Domain Configuration

In order for our simulations to be easily comparable to simulations of existing models of sub-ice shelf cavity circulation, we use an experimental setup based on the configuration created for the Marine Ice Ocean Modeling Inter-comparison Project (MISOMIP; Asay-Davis et al., 2016). Since all simulations in this study are performed on an f -plane, we are free to define the axes of our domain. We define the east and north directions to be the directions of increasing x and y respectively, with the terms “zonal” and “meridional” defined accordingly. The configuration consists of a rectangular domain $L_x = 80$ km long and $L_y = 480$ km wide. The ice shelf is grounded on the southern side of the domain with the ice shelf front at $y = 650$ km.

Table 1
Ocean-Model Parameters

Parameter	Symbol	Value	Unit
Domain length	L_x	80	km
Domain width	L_y	480	km
Horizontal resolution	Δx	2	km
Number of vertical layers	N_l	72	non-dim
Horizontal viscosity	ν_H	6.0	$\frac{m^2}{s}$
Diapycnal viscosity	ν_V	10^{-3}	$\frac{m^2}{s}$
Horizontal diffusivity	ϵ_H	1.0	$\frac{m^2}{s}$
Diapycnal diffusivity	ϵ_V	5×10^{-5}	$\frac{m^2}{s}$
Initial surface temperature	T_t	-1.9	$^{\circ}C$
Initial bottom temperature	T_b	1.0	$^{\circ}C$
Initial surface salinity	S_t	33.8	psu
Initial bottom salinity	S_b	34.7	psu
Maximum ocean depth	H_{ocean}	720	m
Relaxation time of sponge layer	T_{sponge}	0.1	days
Time step for static shelf experiment	dt_{Static}	1,000	s
Time step for iceberg calving experiment	$dt_{Calving}$	10	s

The ice thickness and bottom topography of this setup are shown in Figure 3. The configuration is the same as that of the Ocean0 setup in the MISOMIP, with the following changes:

1. The “calving criteria” used in the MISOMIP study (which states that all points in the ice shelf with thickness less than 100 m are set to zero thickness) has not been used.
2. The ice shelf geometry has been adjusted so that it is symmetric about its meridional center line, and the latitude of the grounding line decreases monotonically, so that the southernmost point on the grounding line is at the center of the domain.

These changes were made in order to make the circulation beneath the ice shelf easier to interpret.

3.2. Ocean Model

The Lagrangian and Eulerian ice shelves are each coupled to the MOM6 ocean model (Hallberg et al., 2012). The ocean model uses a hybrid vertical coordinate system, which blends a sigma-coordinate and a z-coordinate (Stern et al., 2017), implemented using the Arbitrary Lagrangian Eulerian (ALE) method (White et al., 2009). In this hybrid vertical coordinate, model layers bend underneath surface topography (i.e., the ice shelf), as they would in a sigma-coordinate model, and intersect the bottom topography, as they would in a z-coordinate model. Using sigma-coordinates in the upper part of the column allows uniform treatment of the boundary layer in contact with the ice shelf bottom. The model has 72 vertical layers and has a horizontal resolution of $\Delta x = 2$ km. The static ice shelf simulations were repeated using an isopycnal coordinate (without ALE regridding-remapping). The results were qualitatively similar to the hybrid-coordinate results and are therefore not presented here.

The ocean parameters used in the simulations are as specified in the MISOMIP configuration (Asay-Davis et al., 2016) and are shown in Table 1. The simulation is initialized from rest, with horizontally uniform initial ocean temperature and salinity profiles, which vary linearly between specified open-ocean surface and bottom values: $T_{top} = -1.9^{\circ}C$, $T_{bottom} = 1.0^{\circ}C$, $S_{top} = 33.8$ psu, $S_{bottom} = 34.7$. The maximum ocean depth is $H_{ocean} = 720$ m. A sponge layer is used on the northern boundary, which relaxes back to the initial temperature and salinity with a relaxation time scale of $T_{sponge} = 0.1$ days over a distance of 10 km. Melting is set to zero for ocean cells where the ocean column thickness is less than 10 m, as our ice shelf melt parameterization was not designed to handle small ocean thickness.

3.3. Lagrangian Ice Shelf Model

The Lagrangian ice shelf is initialized as 10882 Lagrangian hexagonal elements with sides of length $S = 980$ m. The positions of the hexagonal elements are determined by packing them together in a

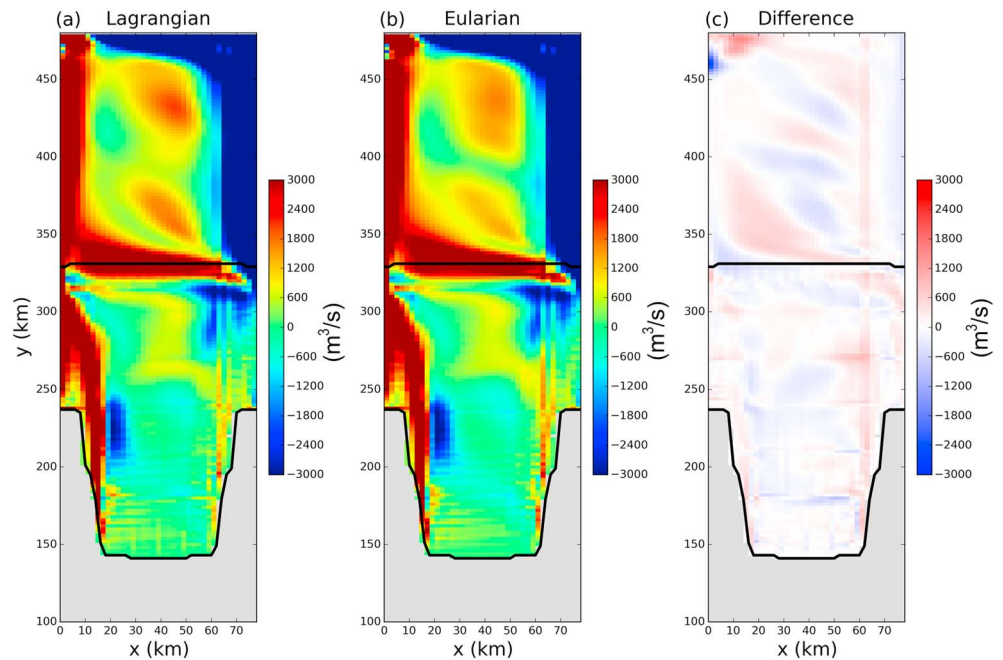


Figure 4. Comparison of Lagrangian and Eulerian ice shelf representations. Time-averaged barotropic stream function in the (a) Lagrangian and (b) Eulerian simulations in the static ice shelf configuration. Panel (c) shows the difference between panels (a) and (b). The time averages are taken over 5 years of model time, beginning at the end of the 5-year spin-up period.

space-filling staggered lattice. Gaps along the boundaries are filled in using smaller elements so that the total ice shelf area is preserved. The initial mass of the ice elements is determined using bilinear interpolation from a prescribed gridded ice mass field.

3.4. Eulerian Ice Shelf Model

The Eulerian ice shelf simulation uses an existing Eulerian ice shelf cavity model (Goldberg et al., 2012; Little et al., 2009), which is an optional module within the MOM6 ocean model. The ice shelf is initialized on the same grid as the ocean model with a horizontal resolution of $\Delta x = 2$ km. The ice shelf thickness field is initialized using the same ice shelf draft used for the Lagrangian model (Figure 3). The melt rates in the Eulerian ice shelf simulation are calculated using the three-equation formulation (Holland & Jenkins, 1999), with the same parameters used to calculate the ice shelf melt rates in the Lagrangian model.

4. Model Verification

In this section we compare the results of the Lagrangian ice shelf model with the results of the traditionally used Eulerian model, run in identical static ice shelf configuration, and demonstrate that the results of the two models are in very close agreement.

The experimental setup for the model verification experiment is based on the Ocean0 MISOMIP experiment (Asay-Davis et al., 2016). In this experiment the ice shelves are thermodynamically active but have a time-invariant thickness. Temperature and salinity fluxes from ice shelf melt drive the circulation within the cavity. A constant wind stress $\vec{\tau} = (\tau_x, \tau_y) = (0.05, 0.05) \frac{N}{m^2}$ is applied to the ocean surface. Note that this wind stress is was not applied in the original MISOMIP experiments but is added here to represent the katabatic winds and to force the iceberg offshore in the nonstatic simulations.

The elements in the Lagrangian ice shelf simulation are held stationary so that the ice shelf is static and comparable to the Eulerian simulation. The models are spun up for 5 years. The analysis is performed on years 6 to 10 of the simulations.

The results of the static ice shelf simulations in both models are qualitatively similar to results presented in Asay-Davis et al. (2016). Melting at the base of the ice shelf drives a circulation within the cavity, and strong

jets are observed at the ice front and along the sides of the domain (Figure 4). A more complete description of the circulation is provided in the supporting information.

We note that the Lagrangian model was intentionally constructed along side the Eulerian model so that two models would produce the similar results when used in a static configuration. That is, since the Lagrangian and Eulerian ice shelf models are coupled to the same ocean model and the ice shelf models use the same parameterization for ice shelf melt, we expect the results of the two models to be the almost the same, with the only differences arising from the interpolation and aggregation schemes (see section 2.4).

The model comparison confirms that the two simulations are almost indistinguishable, as shown by the time-averaged barotropic stream functions (Figure 4). The difference between the Lagrangian and Eulerian barotropic stream functions is 2 orders of magnitude smaller than differences between our MOM6 results and those from POP2x (Asay-Davis et al., 2016). The similarity of the Lagrangian and Eulerian simulations are also reflected in the fact that the simulations have very similar ice shelf melt rates and ocean temperature/salinity profiles (shown in Figures S1 and S2).

The agreement between the Eulerian and Lagrangian simulations confirms that the Lagrangian model is able to simulate sub-ice shelf cavities as well as the Eulerian model does. Having gained confidence in the Lagrangian model, we now explore its unique capabilities.

5. Iceberg Calving Experiment

The Lagrangian ice shelf model developed in this study allows us to simulate an iceberg calving away from the ice shelf and to study what effect this has on the ocean around the iceberg and beneath the ice shelf. Since the Lagrangian iceberg/ice shelf model is fully coupled to the ocean, the iceberg motion affects the ocean hydrography, and the changing ocean conditions feed back onto the ice.

In this section, the Lagrangian ice shelf model is used to simulate a tabular iceberg detaching from the ice shelf, and drifting into the open ocean. The results below show that the calving of a large tabular iceberg can cause significant changes to the ocean stratification and circulation around the iceberg and at the ice shelf front.

5.1. Setup of Iceberg Calving Experiment

The iceberg calving experiment is initialized using the final state of the static Lagrangian ice shelf simulation (i.e., at time $t = 10$ years). When simulating the calving event, we bypass the question of how to prescribe a physical calving law (Alley et al., 2008; Bassis & Jacobs, 2013; Benn et al., 2007; Levermann et al., 2012) by manually breaking off a semicircular iceberg. All ice elements initially within a 14.4-km radius of the center of the ice front are allowed to move freely while the other ice elements continue to be held stationary. Ice elements less than 12 km from the center of the ice front remain bonded together to form a semicircular tabular iceberg. A ring of elements whose distance, d , from the ice front center obeys $12\text{km} \leq d \leq 14.4\text{km}$, are allowed to move freely, but have all their bonds removed.

5.2. Results of Iceberg Calving Experiment

5.2.1. Ocean Response to Iceberg Detachment

After the numerical bonds are broken, a large semicircular tabular iceberg detaches from the ice shelf and begins to drift northward (Figure 2 and Movie S1). The detachment of the iceberg gives rise to a dynamical ocean response, which is shown in the schematic in Figures 5a and 5b, and is described below.

Immediately after calving, the northward motion of the iceberg creates a region of open water at the new calving front, between the ice shelf and the tabular iceberg (Figure 2a). The formation of a region of open ocean behind the iceberg causes a sudden stretching of the water column in the wake of the iceberg, which drives an upwelling throughout the water column. The negative background temperature gradient (cold over warm) means that this upwelling is observed as a warm water anomaly beneath newly formed ice front (Figures 6a and 7a). The warming is observed throughout the water column but is largest near the surface. Similarly, the upwelling leads to increased salinity beneath newly formed ice front (not shown).

The calving event also drives an immediate change in ocean currents at the newly created ice front as the ocean adjusts to the topographic changes. Since the Coriolis parameter is negative (representing the Southern Hemisphere), a stretching of the water column behind the iceberg has to be accompanied by the creation of negative relative vorticity in order for potential vorticity (PV) to be conserved. The creation of negative

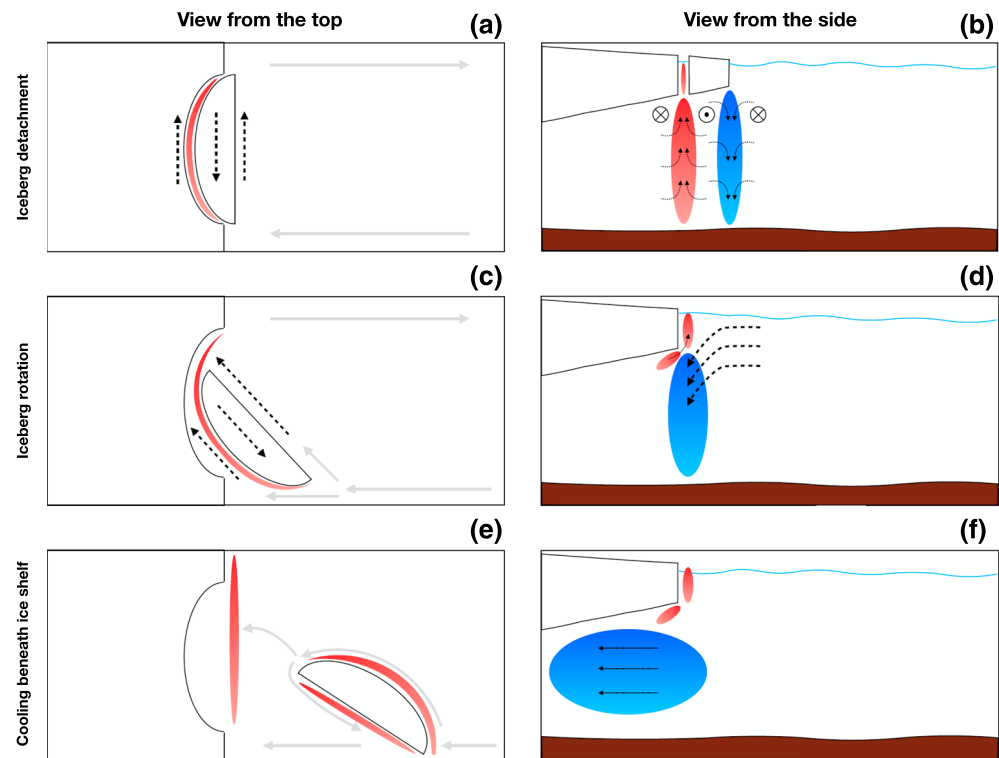


Figure 5. Response of the ocean hydrography to iceberg calving. Cool and warm water anomalies are indicated in blue and red, respectively, and ocean currents are shown using arrows. Stage 1, iceberg detachment (a and b): As the iceberg detaches, water column stretching behind the iceberg causes warm water anomalies behind the iceberg. The conservation of potential vorticity caused by this stretching gives rise to a pair of zonal jets behind and below the iceberg. Similarly, the contracting water column in front of the iceberg creates cool anomalies and drives a zonal jet in front and below the iceberg. Stage 2, iceberg rotation (c and d): As the iceberg drifts away from the ice shelf, it rotates, causing the jets around it to change direction. The newly orientated jet in front of the iceberg drives water toward to ice shelf, which subsducts at the ice front, causing subsurface cooling. Stage 3, cooling below the ice shelf (e and f): As the iceberg moves away from the ice shelf, it interacts with the boundary currents, which are diverted by the presence of the iceberg. At the ice front, the cool water anomalies are advected into the ice shelf cavity, eventually leading to reduced melt rates throughout the cavity. Surface warming (panels a, c, and e): At the surface, the warm water anomalies behind the iceberg after calving (panel a) move with the iceberg as it drifts (panel c) and entirely surround the iceberg (panel e).

relative vorticity along the newly calved ice front gives rise to a pair of oppositely oriented ocean jets running along the ice front. A westward barotropic jet is created to the south of the calving front, and an eastward barotropic jet is created to the north of the calving front (Figures 8a and 9a). The positive gradient in zonal velocity created by this pair of oppositely orientated jets yields the negative relative vorticity.

To the north of the iceberg, the iceberg detachment has the opposite effect on the ocean. The forward movement of the iceberg causes a squeezing of the water column directly in front of the iceberg. This shortening of the water column causes a downwelling in the water column, which is observed as a cool water anomaly in front of the iceberg (Figure 6a). The squeezing of the water column generates positive relative vorticity, so that the total PV is conserved. The positive relative vorticity creates eastward and westward jets to the south and north, respectively, of the northern edge of the iceberg (Figures 8a and 9a). The stretching and squeezing of the water column to the south and north of the iceberg both contribute to the eastward jet that forms directly beneath the iceberg, which plays an important role in driving iceberg motion.

5.2.2. Iceberg Motion

After the iceberg breaks away from the ice shelf, the motion of the iceberg is primarily driven by the combination of wind drag, the Coriolis force, and sea surface height gradients associated with ocean currents around the iceberg. The sea surface height gradient associated with the eastward jet beneath the iceberg drives the iceberg toward the east (Figures 8a and 9a), while the wind and Coriolis force drive the iceberg offshore. Initially, as the iceberg drifts eastward, it collides with the ice shelf, which hinders its motion and

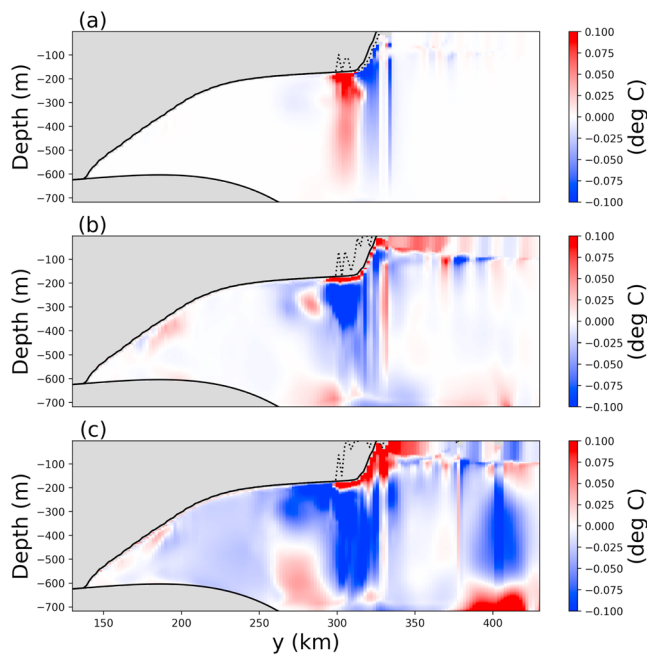


Figure 6. The effects of iceberg calving on sub-ice shelf cavity state. Snapshots of vertical sections of ocean temperature anomaly at $x = 40$ km in the iceberg-calving experiment. The anomalies are relative to precalving temperatures. Snapshots are taken (a) 1, (b) 15, and (c) 50 days after calving. In each panel, the base of the ice before calving and at the time of the snapshot are shown by the solid and dashed black lines, respectively. Positions that were not the ocean interior in both snapshots are masked in gray. The position of the vertical transects is shown by the black dashed lines in Figure 2a.

causes the iceberg to rotate in a counterclockwise direction (Figure 2a). Only once the iceberg has drifted sufficiently far northward to be clear of the ice shelf does it begin to drift toward the east. Once this happens, the iceberg velocity quickly adjusts so that it is approximately equal to the ocean velocity below the iceberg. The iceberg continues to rotate counterclockwise as it drifts northward, until it collides with the boundary of the domain (Figure 2c).

The motion of the iceberg sets the direction of the ocean flow below and around the iceberg, since the ocean has to adjust to topographical changes while conserving PV. This is illustrated, for example, by the change in orientation of the ocean jets running beneath the iceberg that occurs as the iceberg rotates (Figures 8b and 8e). An important consequence of the controlling effect of iceberg topography is the formation of a Taylor Column below the iceberg: The water column below the iceberg is constrained to move at the same speed as the iceberg above, since differential motion would force the water column out from under the iceberg, causing the water column to stretch, and generating PV. This means that the column of water beneath the iceberg is largely separated from the water around the iceberg and strong gradients in temperature, salinity, and velocity can exist at the iceberg edge. In our experiment, a Taylor Column is clearly observed below the iceberg throughout the simulation (Figure 9 and Movie S2).

Once the iceberg reaches the eastern side of the domain, it begins to interact with the boundary of the domain and with the southward boundary current running along the edge of the domain (Figures 2b and 8f). The presence of the iceberg along the eastern boundary impedes the southward boundary current, so that the current has to flow to the west of the iceberg. The diverted current follows the topographic contour created by the iceberg so that it sets up a counterclockwise circulation running

around the iceberg (Figures 8c and 8f). The eastward jet, which was previously positioned beneath the iceberg, shifts to the south and becomes part of the flow directing the boundary current around the iceberg. This counterclockwise circulation around the iceberg remains around the iceberg until the end of the simulation. Interestingly, the iceberg continues to move northward despite the fact that it is moving within a southward flowing boundary current (Figure 9c). This is partly due to the Taylor Column beneath the iceberg, which allows the northward velocity beneath the iceberg to be separated from the southward moving current around the iceberg. The rotation of the iceberg and interaction with the boundary current are summarized in the schematics in Figures 5c and 5e.

Although the limited size of the domain and the presence of its boundaries constrain the motion of the iceberg, making it specific for the chosen geometry, real icebergs are observed to interact with the Antarctic coastline and coastal currents, and our simulations provide insights of potential alterations in the ocean circulation due to such interactions.

5.2.3. Surface Warming and Subsurface Cooling

After the tabular iceberg detaches from the ice shelf, warming is observed throughout the water column to the south of the iceberg (Figure 6a, as discussed above). This warming extends to the ocean surface, resulting in warm sea surface temperature (SST) anomalies at the newly calved ice front and around the southern side of the iceberg (Figures 2 and 7a). In the weeks following calving, part of this warm SST anomaly remains at the ice front, influencing the heat flux into the ice shelf cavity, and some of the SST anomaly drifts with the iceberg into the open ocean (see schematic in Figure 5).

The warm SST anomalies at the ice front persist and strengthen, even once the tabular iceberg has drifted away, as water continues to upwell at the newly formed ice front. Some of this warmed surface water is advected to the west by the westward jet at the ice front (Figure 2c). Once these warmed surface waters reach

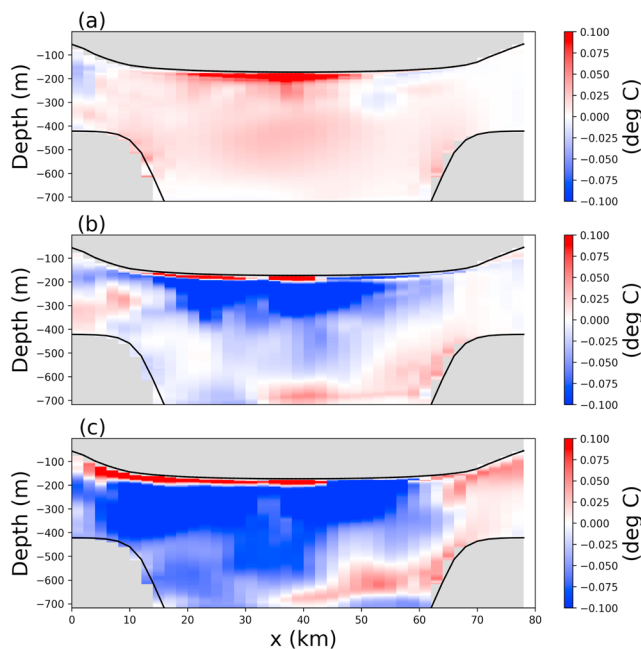


Figure 7. Same as Figure 6, Snapshots of vertical sections of ocean temperature anomaly at $y = 300$ km in the tabular-iceberg-calving experiment. The anomalies are relative to precalving temperatures. Snapshots are taken (a) 1, (b) 15, and (c) 50 days after calving. The position of the vertical transects is shown by the blue dashed lines in Figure 2a.

the western side of the domain, most of this warm anomaly is advected northward following the western boundary, while some of the warmth is forced southward and is able to subduct beneath ice shelf on the western side of the ice shelf front.

The SST anomalies that drift along with the iceberg are initially concentrated along the curved southern side of the iceberg. As the tabular iceberg drifts away from the ice shelf (and begins to rotate), the currents that develop around the iceberg advect this warm SST anomaly counterclockwise around the perimeter of the iceberg so that by 15 days after calving, the SST around the most of the iceberg's perimeter is anomalously warm (Figure 2). As the iceberg drifts further into the open ocean, the strength of the warm SST anomalies around the iceberg's perimeter increases. The warmed surface waters around the iceberg mix with the ambient surface water, leaving a trail of warmed surface water, which maps out the wake of the iceberg.

As discussed above, the downwelling on the northern side of the iceberg, observed immediately after calving, leads to a cooling/freshening of the water column beneath and to the north of the iceberg (Figures 6a and 7a). As the iceberg drifts away from the ice shelf, the cool water anomalies remain beneath the iceberg, traveling with the iceberg into the open ocean, leaving a trail of cool subsurface temperature anomalies, which maps out the (subsurface) wake of the iceberg (not shown). The pattern of warm surface anomalies around the iceberg, and cool subsurface anomalies around the iceberg, is clearly visible throughout the simulation (Figure 9d) and suggests continued vertical mixing around the iceberg perimeter as it drifts into the open ocean.

About 5 days after calving, as the iceberg begins to rotate counterclockwise, the jet to the north of the iceberg begins to drive the cool water anomaly toward the ice front (Figure 8b). The strong jet moving toward the ice front causes water to subduct beneath the ice front, leading to further cool subsurface anomalies. Below the depth of the ice shelf, the cool water anomalies are stronger than the warm water anomalies caused by the initial water column stretching. The subsurface negative temperature anomalies strengthen over time, and within a month of the calving event, the negative anomalies occupy most of the water column close to the ice front (Figures 7b and 7c). This subsurface cooling at the ice front is the most prominent temperature response observed in our iceberg calving experiments (see schematic in Figure 5d and Movie S1). Similar subsurface cooling at the ice front was observed in other experiments using different sizes and shapes for the calving iceberg (not shown). The subsurface cooling and warm surface temperature anomalies discussed above are accompanied by a freshening at depth and an increase in surface salinity (not shown).

The zonal current along the ice front drives the cool anomaly to the west, causing an enhancement of the cool anomalies on the western side of the ice shelf front (Figure 7c). Most of the subsurface cooling occurs outside of the ice shelf cavity, as the dynamical barrier caused by the ice shelf inhibits exchange of water across the ice front. However, over time, an increasing amount of cooler water is gradually able to enter the ice shelf cavity and be advected below the ice shelf (Figure 6c).

5.2.4. Sub-Ice Shelf Cavity Circulation

The combination of cool subsurface temperature anomalies and elevated ocean velocities at the ice front results in a temperature flux across the ice front, as cool temperature anomalies to enter the ice shelf cavity (Figures 6c and 5f). Once the cooler water has entered the ice shelf cavity, the anomalies spread southward within the ice shelf cavity, eventually reaching all the way to the grounding line. As the cool water spreads into the cavity, it mixes with the water within the ice shelf cavity, causing a reduction in the strength of the anomaly toward the grounding line (Figure 6c).

The cooling of the water inside the ice shelf cavity after calving leads to a reduction of melting at the base of the ice shelf (Figure 10). This occurs over a wide area extending from the newly calved ice front, all the way toward the grounding line. The negative melt rate anomalies increase over time, as more cold water enters the ice shelf cavity. The strongest negative anomalies are observed near the ice front, while the strength of

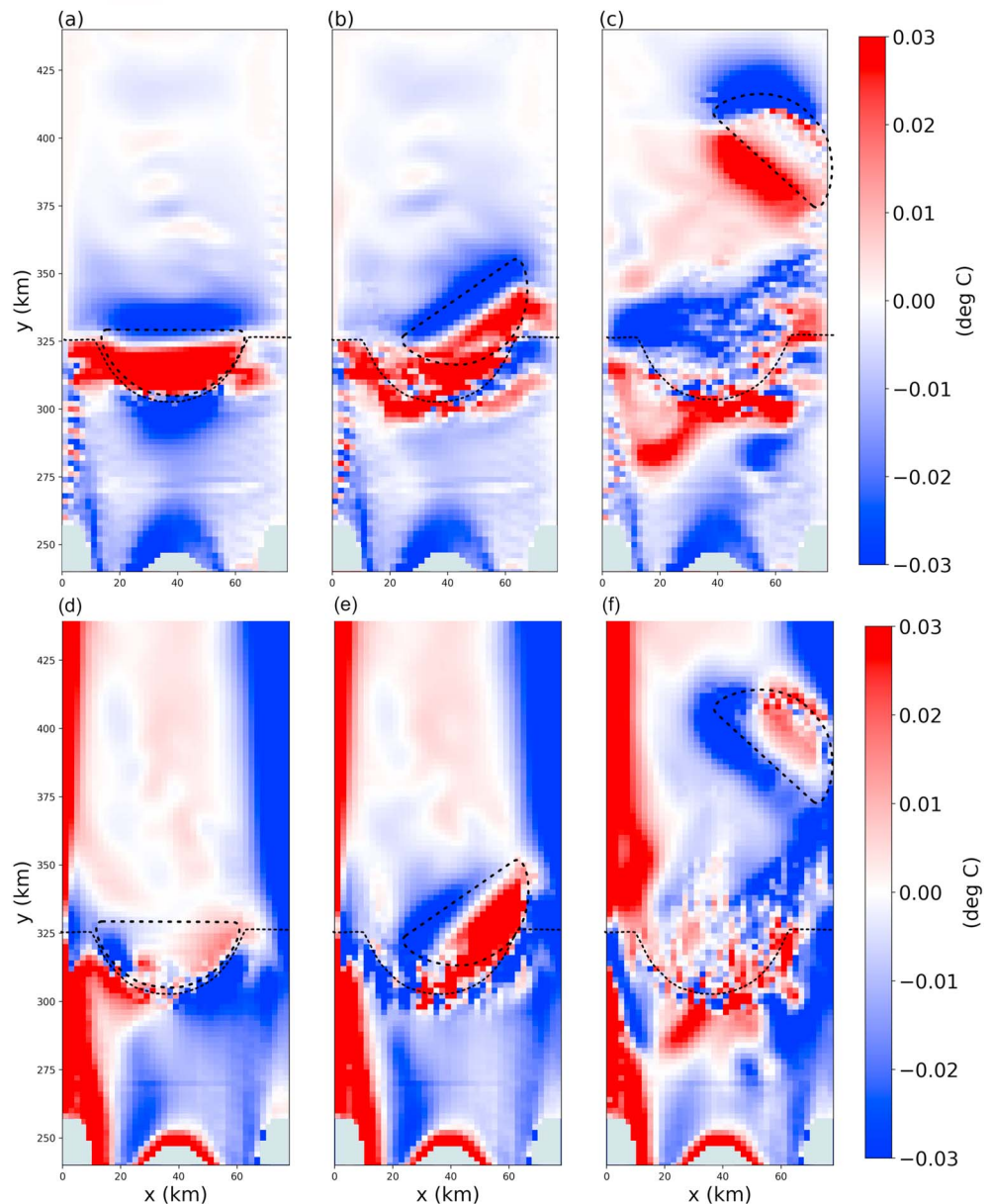


Figure 8. Ocean velocity below drifting iceberg. Snapshots of the (a–c) zonal and (d–f) meridional velocity at $z = 197.5$ m in the iceberg-calving experiment. Snapshots are taken (a and d) 1, (b and e) 7, and (c and f) 50 days after calving. The dashed lines show the perimeter of the iceberg and the postcalving ice front.

the negative melt rate anomalies are reduced toward the grounding line. The reduction in melt rates are up to 0.5 m per year, which is small compared to the mean melt rates near the grounding line but is a substantial fraction of the melt at intermediate depths (Figure S4).

Near the ice front, the competing effects of warm surface water subducting beneath the ice shelf on the flanks of the domain, and the cool water entering the ice shelf in the center of the domain, lead to a complex of pattern of positive and negative melt rate anomalies within 20 km of the ice front (Figure 10).

5.2.5. Steady State Hydrography

The presence of a northern boundary in our simulation means that we are unable to entirely remove the iceberg from the domain and observe the system approaching a new equilibrium state. However, a comparison between the iceberg-calving simulation and an “equilibrium-shelf simulation” (where the model was spun up with the iceberg removed from the start) shows that after 60 days, the hydrography inside the ice-shelf

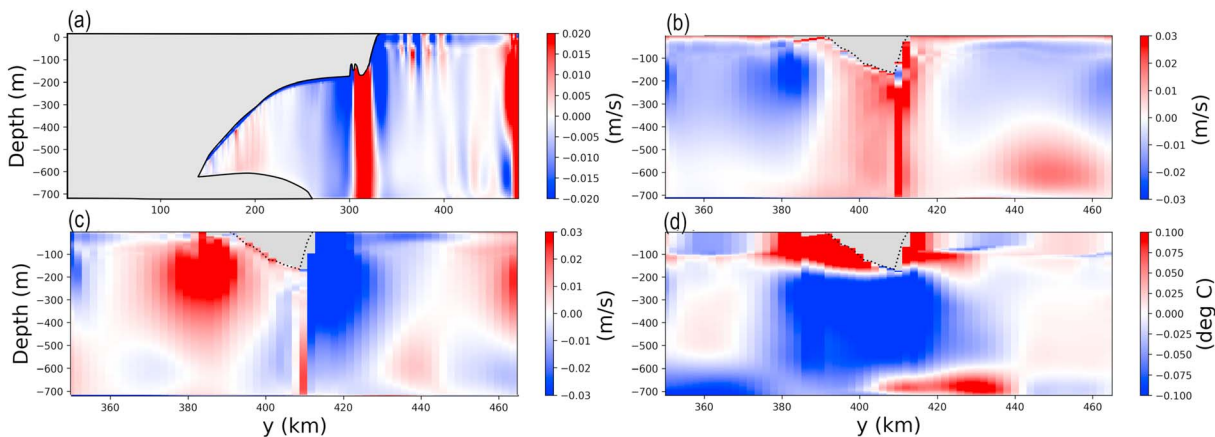


Figure 9. Taylor column below iceberg. Panel (a) shows a snapshot of vertical section of zonal velocity at $x = 40$ km in the iceberg-calving experiment 1 day after calving. An eastward jet is observed beneath the iceberg, and westward jets are observed to the north and south of the iceberg. Panels (b), (c), and (d) show snapshots of hydrography around the iceberg 50 days after calving. The snapshots show vertical sections of ocean (b) zonal velocity, (c) meridional velocity, and (d) temperature anomaly at $x = 60$ km in the tabular-iceberg-calving experiment. The anomalies are relative to precalving temperatures. The position of the vertical transect in panel (a), and panels (b), (c), and (d) are shown by the black dashed lines in Figures 2a and 2c, respectively.

cavity in the iceberg-calving simulation appears to be qualitatively similar to equilibrium-shelf simulation steady state (see Figure S5). This suggests that the processes occurring at the ice front directly after calving are transient processes, which allow the system to move toward a steady state that is largely controlled by the ice shelf geometry. Since the ice shelf geometry in our simulation is highly idealized and is in a closed domain, it is unclear whether the adjustment time scale seen here is relevant to real-world ice shelves.

Although the processes described above (e.g., formation of an open water region immediately after the iceberg detachment, upwelling and downwelling on the opposite sides of the iceberg, and alteration of the PV) have been observed in simulations with a particular size of the calved iceberg, additional simulations with different size and shaped icebergs suggest that that these processes are general for calving of tabular icebergs (i.e., icebergs whose horizontal extent is much larger than the vertical one). The magnitudes of these pro-

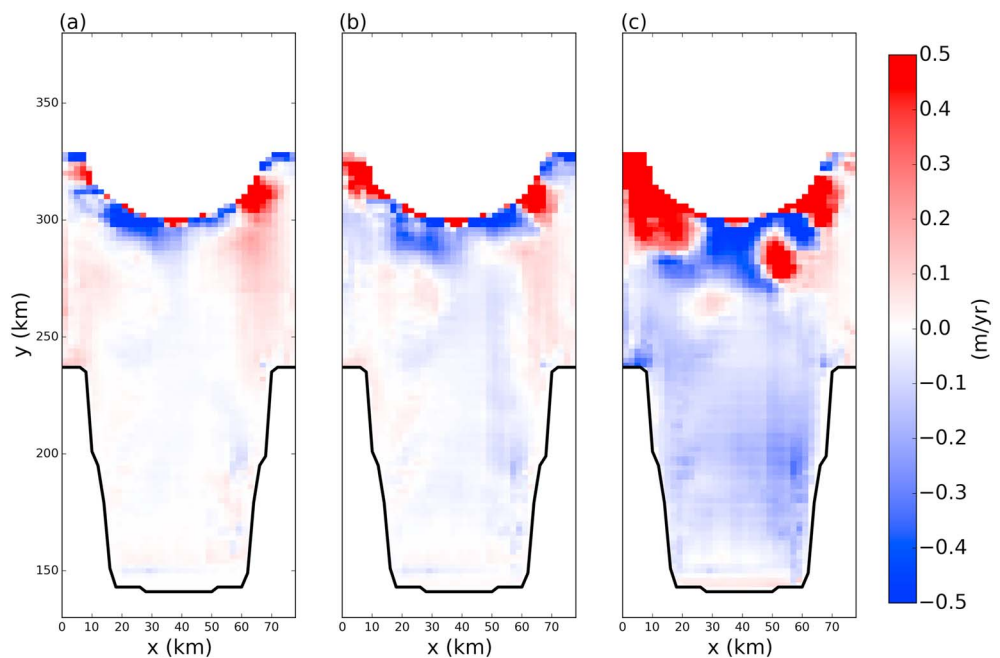


Figure 10. Evolution of ice shelf melt rates after calving. Snapshots of the melt rate anomaly, at the ice shelf base in the tabular iceberg-calving simulation. The anomalies are relative to precalving melt rates. Snapshots are taken (a) 7, (b) 15, and (c) 50 days after calving.

cesses are most likely different for icebergs with different shapes and dimensions. Exploration of the effects of these processes will be the subject of a future study.

In the absence of direct hydrographic observations around the calving iceberg or at the newly formed ice shelf front after its immediate detachment, it is difficult to assess the accuracy of the simulated changes in the ocean stratification during a calving event. In situ oceanographic measurements in the vicinity of the calving iceberg similar to those collected around a small iceberg in the Weddell Sea (Morison & Goldberg, 2012) will be very useful for validating the model behavior and improving understanding of the oceanographic response to calving in general.

6. Summary

The simulations presented above demonstrate that the calving of a large tabular iceberg can cause significant changes to the ocean stratification and circulation around the iceberg and at the ice front. Although the idealized geometry of the simulations makes it difficult to compare the results directly to real-world observations, a number of robust features were observed in this iceberg-calving simulation, which could have real-world analogs.

- 1. Dynamical response of ocean to iceberg calving.** As the iceberg detaches from the ice shelf, there is an immediate dynamical ocean response: A stretching of the water column directly behind the iceberg gives rise to ocean upwelling, which leads to a warm, salty anomaly being created at the newly calved ice front. Conservation of PV requires that this ocean column stretching gives rise to the formation of a pair of oppositely oriented jets, which form directly behind the iceberg. A similar (and oppositely signed) phenomenon occurs in front of the iceberg, where a squeezing of the water column leads to downwelling, a cooling/freshening of the water column and a pair of oppositely oriented jets being created along the front side of the iceberg (see schematic in Figures 5a and 5b).
- 2. The influence of iceberg topography.** The iceberg topography controls the ocean below it. This is demonstrated by the shifting of ocean jets below the iceberg in response to the iceberg motion. It is also demonstrated by the Taylor column that forms directly below the iceberg. This Taylor column follows the iceberg as it drifts into the open ocean and leads to a separation between the ocean properties below the iceberg and the ambient ocean conditions. This provides a mechanism for lateral transport of water masses from near the calving front and, if the iceberg crosses the continental shelf break, could potentially transport water masses off the continental shelf out into the open ocean.
- 3. Localized changes in ocean hydrography around the iceberg.** The calving and motion of the iceberg have a large and complex effect on ocean temperature and salinity around the iceberg and at the calving front. In our experiment, warmed water surrounds the iceberg as it drifts away from the ice shelf and maps out a trail of warm surface anomalies in the wake of the iceberg. Similarly, cooler waters are observed below the iceberg and map out a trail of cool subsurface anomalies in the iceberg wake.
- 4. Interaction between iceberg and ocean currents.** As the iceberg drifts away from the ice shelf, it can interact with the ocean currents around the ice shelf. In our simulation, the iceberg impedes the ocean current coming toward the ice shelf, which is diverted around the iceberg and sets up a new circulation around the iceberg. This change in circulation directs a current toward the center of the ice shelf front, where the water subducts, causing large cool anomalies at the ice front (see schematic in Figure 5). While this result is specific to the particular experimental setup used in our experiment, it suggests a more general result that drifting icebergs can interact and divert local ocean currents around the ice shelf. If these local currents are moving toward or away from the ice shelf, this can alter the heat flux into the ice shelf cavity.
- 5. Iceberg calving can affect sub-ice shelf temperatures and melt rates.** Large changes in ocean properties that occur at the ice front following the iceberg calving can directly affect the temperature flux into the ice shelf cavity, which in turn alter the sub-ice shelf melt rates. In our experiment, the cool surface water subducting beneath the ice shelf lead to reduced melt rates beneath the ice shelf. This decrease in melt rate extends far into the ice shelf cavity.
- 6. The influence of the ice-shelf geometry.** Once the iceberg has drifted far away from the ice shelf cavity, the conditions and melt rates within the ice shelf cavity appear to be converge toward values similar to those in simulations run with the iceberg removed from the start. This result suggests that the melt rates inside the ice shelf cavity are largely controlled by the ice shelf geometry. The changes in ocean conditions caused by the interaction with the iceberg appear to be transient adjustment processes.

Further work is needed to understand how these features are expressed in real-world ice shelf cavities, with varying geometries, forcing, and stratification. Nonetheless, the results presented in this study suggest that for many calving events, the interaction between the calving iceberg and the surrounding ocean is likely to play an important role in determining the hydrography around the iceberg and could also have first-order transient effects on the hydrography at the ice front and within the ice shelf cavity.

Acknowledgments

We would like to thank the Associate Editor Laurie Padman and reviewers Xylar Asay-Davis and Dan Goldberg, for valuable comments and useful suggestions that greatly improved the manuscript. This study is supported by awards NA08OAR4320752 and NA13OAR439 from the National Oceanic and Atmospheric Administration, U.S. Department of Commerce. The statements, findings, conclusions, and recommendations are those of the authors and do not necessarily reflect the views of the National Oceanic and Atmospheric Administration or the U.S. Department of Commerce. The simulations in this paper can be reproduced using the model code and experimental setups found at https://github.com/sternalon/Iceberg_repository, and the data used to produce the figures in this paper have been submitted to the NSIDC data center.

References

- Alley, R. B., Horgan, H. J., Joughin, I., Cuffey, K. M., Dupont, T. K., Parizek, B. R., et al. (2008). A simple law for ice-shelf calving. *Science*, 322(5906), 1344–1344. <https://doi.org/10.1126/science.1162543>
- Asay-Davis, X. S., Cornford, S. L., Durand, G., Galton-Fenzi, B. K., Gladstone, R. M., Gudmundsson, G. H., et al. (2016). Experimental design for three interrelated marine ice sheet and ocean model intercomparison projects: MISMIP v. 3 (MISMIP+), ISOMIP v. 2 (ISOMIP+) and MISOMIP v. 1 (MISOMIP1). *Geoscientific Model Development*, 9(7), 2471–2497. <https://doi.org/10.5194/gmd-9-2471-2016>
- Bassis, J. N., & Jacobs, S. (2013). Diverse calving patterns linked to glacier geometry. *Nature Geoscience*, 6(10), 833–836. <https://doi.org/10.1038/ngeo1887>
- Benn, D. I., Warren, C. R., & Mottram, R. H. (2007). Calving processes and the dynamics of calving glaciers. *Earth-Science Reviews*, 82(3), 143–179. <https://doi.org/10.1016/j.earscirev.2007.02.002>
- Biddle, L. C., Kaiser, J., Heywood, K. J., Thompson, A. F., & Jenkins, A. (2015). Ocean glider observations of iceberg-enhanced biological production in the northwestern Weddell Sea. *Geophysical Research Letters*, 42, 459–465. <https://doi.org/10.1002/2014GL062850>
- Bigg, G. R., Wadley, M. R., Stevens, D. P., & Johnson, J. A. (1997). Modelling the dynamics and thermodynamics of icebergs. *Cold Regions Science and Technology*, 26(2), 113–135. [https://doi.org/10.1016/S0165-232X\(97\)00012-8](https://doi.org/10.1016/S0165-232X(97)00012-8)
- DeRydt, J., & Gudmundsson, G. H. (2016). Coupled ice shelf-ocean modeling and complex grounding line retreat from a seabed ridge. *Journal of Geophysical Research: Earth Surface*, 121, 865–880. <https://doi.org/10.1002/2015JF003791>
- Depoorter, M. A., Bamber, J. L., Griggs, J. A., Lenaerts, J. T. M., Ligtenberg, S. R. M., van den Broeke, M. R., & Moholdt, G. (2013). Calving fluxes and basal melt rates of Antarctic ice shelves. *Nature*, 502(7469), 89–92. <https://doi.org/10.1038/nature12567>
- Determann, J., & Gerdes, R. (1994). Melting and freezing beneath ice shelves: Implications from a three-dimensional ocean-circulation model. *Annals of Glaciology*, 20, 413–419. <https://doi.org/10.3189/172756494794587591>
- Gladish, C. V., Holland, D. M., Holland, P. R., & Price, S. F. (2012). Ice-shelf basal channels in a coupled ice/ocean model. *Journal of Glaciology*, 58(212), 1227–1244. <https://doi.org/10.3189/2012JG12J003>
- Gladstone, R. M., Bigg, G. R., & Nicholls, K. W. (2001). Iceberg trajectory modeling and meltwater injection in the Southern Ocean. *Journal of Geophysical Research*, 106(C9), 19,903–19,915. <https://doi.org/10.1029/2000JC000347>
- Goldberg, D. N., Little, C. M., Sergienko, O. V., Gnanadesikan, A., Hallberg, R., & Oppenheimer, M. (2012). Investigation of land ice-ocean interaction with a fully coupled ice-ocean model: 1. Model description and behavior. *Journal of Geophysical Research*, 117, F02037. <https://doi.org/10.1029/2011JF002246>
- Grosfeld, K., Gerdes, R., & Determann, J. (1997). Thermohaline circulation and interaction between ice shelf cavities and the adjacent open ocean. *Journal of Geophysical Research*, 102(C7), 15,595–15,610. <https://doi.org/10.1029/97JC00891>
- Grosfeld, K., & Sandhger, H. (2004). The evolution of a coupled ice shelf-ocean system under different climate states. *Global and Planetary Change*, 42(1), 107–132. <https://doi.org/10.1016/j.gloplacha.2003.11.004>
- Hallberg, R., Adcroft, A., Dunne, J. P., Krasting, J. P., & Stouffer, R. J. (2012). Sensitivity of twenty-first-century global-mean steric sea level rise to ocean model formulation. *Journal of Climate*, 26(9), 2947–2956. <https://doi.org/10.1175/JCLI-D-12-00506.1>
- Hellmer, H. H., & Olbers, D. J. (1989). A two-dimensional model for the thermohaline circulation under an ice shelf. *Antarctic Science*, 1(4), 325–336. <https://doi.org/10.1017/S0954102089000490>
- Holland, P. R., & Feltham, D. L. (2006). The effects of rotation and ice shelf topography on frazil-laden ice shelf water plumes. *Journal of Physical Oceanography*, 36(12), 2312–2327. <https://doi.org/10.1175/JPO2970.1>
- Holland, D. M., & Jenkins, A. (1999). Modeling thermodynamic ice-ocean interactions at the base of an ice shelf. *Journal of Physical Oceanography*, 29(8), 1787–1800. [https://doi.org/10.1175/1520-0485\(1999\)029<1787:MTIOIA>2.0.CO;2](https://doi.org/10.1175/1520-0485(1999)029<1787:MTIOIA>2.0.CO;2)
- Holland, D. M., & Jenkins, A. (2001). Adaptation of an isopycnal coordinate ocean model for the study of circulation beneath ice shelves. *Monthly Weather Review*, 129(8), 1905–1927. [https://doi.org/10.1175/1520-0493\(2001\)129<1905:AOAICO>2.0.CO;2](https://doi.org/10.1175/1520-0493(2001)129<1905:AOAICO>2.0.CO;2)
- Levermann, A., Albrecht, T., Winkelmann, R., Martin, M. A., Haseloff, M., & Joughin, I. (2012). Kinematic first-order calving law implies potential for abrupt ice-shelf retreat. *The Cryosphere*, 6(2), 273–286. <https://doi.org/10.5194/tc-6-273-2012>
- Little, C. M., Gnanadesikan, A., & Oppenheimer, M. (2009). How ice shelf morphology controls basal melting. *Journal of Geophysical Research*, 114, C12007. <https://doi.org/10.1029/2008JC005197>
- Losch, M. (2008). Modeling ice shelf cavities in a z coordinate ocean general circulation model. *Journal of Geophysical Research*, 113, C08043. <https://doi.org/10.1029/2007JC004368>
- MacAyeal, D. R. (1984). Thermohaline circulation below the Ross Ice Shelf: A consequence of tidally induced vertical mixing and basal melting. *Journal of Geophysical Research*, 89(C1), 597–606. <https://doi.org/10.1029/JC089iC01p00597>
- Marsh, R., Ivchenko, V. O., Skliris, N., Alderson, S., Bigg, G. R., Madec, G., et al. (2015). NEMOICB (v1.0): interactive icebergs in the NEMO ocean model globally configured at eddy-permitting resolution. *Geoscientific Model Development*, 8(5), 1547–1562. <https://doi.org/10.5194/gmd-8-1547-2015>
- Martin, T., & Adcroft, A. (2010). Parameterizing the fresh-water flux from land ice to ocean with interactive icebergs in a coupled climate model. *Ocean Modelling*, 34(3), 111–124. <https://doi.org/10.1016/j.ocemod.2010.05.001>
- Morison, J., & Goldberg, D. (2012). A brief study of the force balance between a small iceberg, the ocean, sea ice, and atmosphere in the Weddell Sea. *Cold Regions Science and Technology*, 76–77, 69–76. <https://doi.org/10.1016/j.coldregions.2011.10.014>
- Rignot, E., Jacobs, S., Mouginot, J., & Scheuchl, B. (2013). Ice-shelf melting around antarctica. *Science*, 341(6143), 266–270. <https://doi.org/10.1126/science.1235798>
- Robinson, N. J., & Williams, M. J. M. (2012). Iceberg-induced changes to polynya operation and regional oceanography in the southern Ross Sea, Antarctica, from in situ observations. *Antarctic Science*, 24(5), 514–526. <https://doi.org/10.1017/S0954102012000296>
- Sergienko, O. V. (2013). Basal channels on ice shelves. *Journal of Geophysical Research: Earth Surface*, 118, 1342–1355. <https://doi.org/10.1002/jgrf.20105>

- Seroussi, H., Nakayama, Y., Larour, E., Menemenlis, D., Morlighem, M., Rignot, E., & Khazendar, A. (2017). Continued retreat of Thwaites Glacier, West Antarctica, controlled by bed topography and ocean circulation. *Geophysical Research Letters*, *44*, 6191–6199. <https://doi.org/10.1002/2017GL072910>
- Smith, K. L., Robison, B. H., Helly, J. J., Kaufmann, R. S., Ruhl, H. A., Shaw, T. J., et al. (2007). Free-drifting icebergs: Hot spots of chemical and biological enrichment in the Weddell Sea. *Science*, *317*(5837), 478–482. <https://doi.org/10.1126/science.1142834>
- Stern, A. A., Adcroft, A., & Sergienko, O. (2016). The effects of Antarctic iceberg calving-size distribution in a global climate model. *Journal of Geophysical Research: Oceans*, *121*, 5773–5788. <https://doi.org/10.1002/2016JC011835>
- Stern, A. A., Adcroft, A., Sergienko, O., & Marques, G. (2017). Modeling tabular icebergs submerged in the ocean. *Journal of Advances in Modeling Earth Systems*, *9*, 1948–1972. <https://doi.org/10.1002/2017MS001002>
- Stern, A. A., Johnson, E., Holland, D. M., Wagner, Tillj. W., Wadhams, P., Bates, R., et al. (2015). Wind-driven upwelling around grounded tabular icebergs. *Journal of Geophysical Research: Oceans*, *120*, 5820–5835. <https://doi.org/10.1002/2015JC010805>
- Timmermann, R., & Goeller, S. (2017). Response to FilchnerRonne Ice Shelf cavity warming in a coupled oceanice sheet model Part 1: The ocean perspective. *Ocean Science*, *13*(5), 765–776. <https://doi.org/10.5194/os-13-765-2017>
- Vernet, M., Smith, K., Cefarelli, A., Helly, J., Kaufmann, R., Lin, H., et al. (2012). Islands of ice: Influence of free-drifting antarctic icebergs on pelagic marine ecosystems. *Oceanography*, *25*(3), 38–39. <https://doi.org/10.5670/oceanog.2012.72>
- Wagner, T. J. W., Dell, R. W., Eisenman, I., Keeling, R. F., Padman, L., & Severinghaus, J. P. (2018). Wave inhibition by sea ice enables trans-Atlantic ice rafting of debris during Heinrich events. *Earth and Planetary Science Letters*, *495*(65), 157–163. <https://doi.org/10.1016/j.epsl.2018.05.006>
- White, L., Adcroft, A., & Hallberg, R. (2009). High-order regridding-remapping schemes for continuous isopycnal and generalized coordinates in ocean models. *Journal of Computational Physics*, *228*(23), 8665–8692. <https://doi.org/10.1016/j.jcp.2009.08.016>